Sensors & Diagnostics

CRITICAL REVIEW

View Article Online
View Journal | View Issue

Cite this: *Sens. Diagn.*, 2023, **2**, 492

NIR-II semiconducting polymers for *in vivo* high-resolution imaging and theranostics

Xiaoying Kang,†[a] Shuai Yin,†[ab] Jianwen Song,[a] Yuan Zhang[a] and Ji Qi *[a]

Precision medicine calls for accurate diagnostic and therapeutic methods that could increase disease sensing and treatment outcome. The second near-infrared (NIR-II, 1000–1700 nm) window has attracted considerable attention because as the light–tissue interaction such as scattering and reflection, absorption and autofluorescence significantly decreases, it enables excellent penetration depth and spatial resolution. Semiconducting polymers (SPs) possess the merits of good stability, easily tunable structures and properties, and potential degradation, holding great potential for NIR-II biomedical applications. In this minireview, we summarize the recent advances in SPs with NIR-II fluorescence emission for precise diagnostics and theranostics. The development and emerging strategies for obtaining high-brightness NIR-II SPs are discussed. NIR-II SPs with other functions including photoacoustic imaging, photothermal therapy, photodynamic therapy and immunotherapy for disease theranostics are illustrated. Biomedical applications such as *in vivo* high-resolution angiography, brain imaging, and various phototheranostic modalities are also highlighted. This review aims to provide guidance for designing high-performance NIR-II SPs to realize maximized effectiveness of various bio-applications, and it will also provide comprehensive understanding about the chemical structure–photophysical property–biomedical application relationships of organic/polymer phototheranostic materials.

Received 29th December 2022,
Accepted 2nd March 2023

DOI: 10.1039/d2sd00234e

rsc.li/sensors

1. Introduction

Precision medicine calls for accurate diagnostic and therapeutic methods that could help to increase disease detection and treatment outcome.[1–3] Compared with the conventional clinically used techniques such as ultrasound, computed tomography (CT), and magnetic resonance imaging (MRI), fluorescence imaging has attracted considerable attention in recent years due to its salient advantages of low cost, real-time monitoring, noninvasive signature, and portable equipment.[4–6] The light–tissue interaction greatly influences the *in vivo* imaging depth and quality, and is significantly decreased due to the bathochromic shift of light wavelength.[7,8] In comparison with the UV-visible region, the first near-infrared (NIR) spectral region (NIR-I, 700–900 nm) has been considered as a promising window for *in vivo* imaging for reduced autofluorescence and self-absorption. Recently, the second NIR (NIR-II, 1000–1700 nm) window has attracted increasing interest because as the light scattering and reflection, absorption and autofluorescence would decrease to a very low level (Fig. 1), it enables excellent tissue penetration depth and spatial resolution.[9–15] NIR-II imaging is thus considered as a highly promising modality for precise disease diagnostics and theranostics.

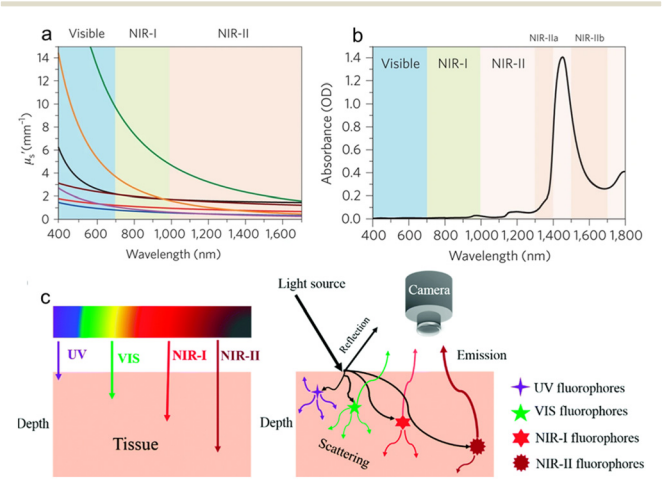

Fig. 1 a) The scattering coefficients of different wavelengths covering the visible, NIR-I and NIR-II windows. b) Absorption spectrum of water in the spectral range of 400–1800 nm. c) Schematic illustration of tissue penetration depth and light–tissue interaction of different wavelengths. Reproduced with permission Copyright©2018, The Royal Society of Chemistry.[15]

[a] *State Key Laboratory of Medicinal Chemical Biology, Frontiers Science Center for Cell Responses, Key Laboratory of Bioactive Materials, Ministry of Education, and College of Life Sciences, Nankai University, Tianjin 300071, China.*
E-mail: qiji@nankai.edu.cn
[b] *School of Pharmacy, Nantong University, Nantong 226001, China*
† X. Kang and S. Yin contributed equally to this work.

A lot of emitters have been developed for NIR-II imaging applications including carbon nanotubes (CNTs), quantum dots (QDs), rare earth metal-doped nanomaterials, organic dyes and semiconducting polymers (SPs).[16–20] Every kind of material has its intrinsic advantages and disadvantages. SPs possess the merits of good stability, easily tunable chemical structures and properties, and potential degradation, gaining a great deal of interest for biomedical applications.[21–23] The strategies to tune the electronic bandgaps of SPs mainly include the extension of conjugation and the donor–acceptor (D–A) structure.[24–29] As compared with the small molecule counterparts, SPs have largely extended conjugation length, and thus the bandgap can be significantly decreased in the high molecular weight polymers.[30,31] The D–A strategy where the electron-donating and electron-withdrawing units are alternately arranged along the polymer backbone is efficient in reducing the bandgap. The electronic energy hybridization of D and A units would result in decreased lowest unoccupied molecular orbital (LUMO) and increased highest occupied molecular orbital (HOMO) energy levels, and thus a low-energy intramolecular charge transfer (ICT) absorption band could be obtained.[32–34] Aside from the conjugated backbone alteration, subtle modification of the substituted groups may also impact the photophysical properties.[35–38] Although SPs could have very small bandgaps and strong NIR absorption, the development of high-brightness candidates is still less than satisfactory because the strong intermolecular interaction such as π–π stacking and interchain entanglement may cause serious fluorescence quenching in the aggregate state.[39–42] Most SPs possess a conjugated backbone structure and hydrophobic nature, so they have to be fabricated into nanoparticles (NPs) to provide good water solubility and biocompatibility. Therefore, the aggregation-caused quenching (ACQ) effect becomes an intractable issue for SPs. To tackle this problem, strategies such as anti-ACQ and aggregation-induced emission (AIE) have emerged as promising options to obtain highly bright NIR-II SP emitters.[43–47]

The energy bandgaps of NIR-II SPs are usually about or lower than 1.5 eV, thus the nonradiative decay process may become inevitable according to the energy bandgap law that the large vibrational overlap between the ground state and the excited state in small-bandgap chromophores would accelerate the nonradiative decays.[48–51] As a result, the full utilization of the "useless" energy would give rise to additional diagnostic and therapeutic functions.[52,53] The nonradiative thermal deactivation would generate heat, which can be employed for other biological applications such as photothermal therapy (PTT) and photoacoustic (PA) imaging. In addition, some SPs may also possess photodynamic therapy (PDT) properties where singlet oxygen ($^1O_2$) and/or reactive oxygen species (ROS) could be generated upon light irradiation.[54,55] Since SPs are composed of macromolecules with different molecular weights, their energy levels would disperse in a wide range, and there would be more energy distribution of the excited singlet states (S_n) and triplet state (T_n), which thus results in decreased ΔE_{ST} (the energy gap between S_n and T_n states) and promotes the intersystem crossing (ISC) process.[56,57] The properties of SPs such as fluorescence, PA, PTT and PDT can be regulated through facile chemical synthesis and structure modification, boosting various biomedical applications.

During the last several years, significant progress has been made in developing NIR-II SPs with different properties for diagnostics and other bio-applications. NIR-II SPs have been used in many biological fields such as fluorescence imaging, PA imaging, chemiluminescence imaging and various therapy modes, and the combination of them.[58–62] For the limited space, in this review, we will focus on the recent advances in SPs with NIR-II fluorescence emission for biomedical applications. The strategies of building high-performance NIR-II fluorescence SPs through chemical structure optimization and their applications for *in vivo* high-contrast imaging and diagnostics will be discussed. SPs with both NIR-II fluorescence and other therapeutic functions for disease theranostic applications will be illustrated. Biomedical applications such as *in vivo* high-resolution angiography, precise brain imaging, phototheranostic integration of fluorescence diagnostics and PTT, and immunotherapy will also be highlighted. This review will provide guidance for designing high-performance NIR-II SPs to realize maximized effectiveness of bio-applications, and it will also provide comprehensive understanding about the chemical structure–property–biomedical application relationships of organic phototheranostic materials.

2. High-performance NIR-II SPs for high-resolution *in vivo* fluorescence imaging and angiography

Small molecular dyes are more used in the NIR-II biomedical field than polymers, which is probably because the conventional dyes with various colours and response wavelengths are easily available.[63–65] NIR-II SPs have shown great promise for NIR-II fluorescence imaging applications in the last several years, which is mainly promoted by the development of new polymers with excellent performance. The first trial of SPs for *in vivo* NIR-II fluorescence imaging can be traced back to 2014. Dai *et al.* reported a low-bandgap SP for ultrafast and high-resolution NIR-II fluorescence imaging.[66] They firstly designed and synthesized a D–A copolymer (pDA) with benzo[1,2-*b*:3,4-*b*′]difuran and fluorothieno-[3,4-*b*]thiophene as the D and A moieties, respectively (Fig. 2a). The polymer pDA was derived from photovoltaic materials, so it had strong NIR absorption ability.[67,68] In order to increase the water solubility and biological compatibility, pDA was coated with amphiphilic polymer 1,2-distearoyl-*sn*-glycero-3-phosphoethanolamine-*N*-[methoxy(polyethyleneglycol)] (DSPE-PEG) to obtain uniform spherical pDA-PEG NPs. The absorption wavelength of pDA-PEG in water was 645 nm, and the NPs had a large Stokes

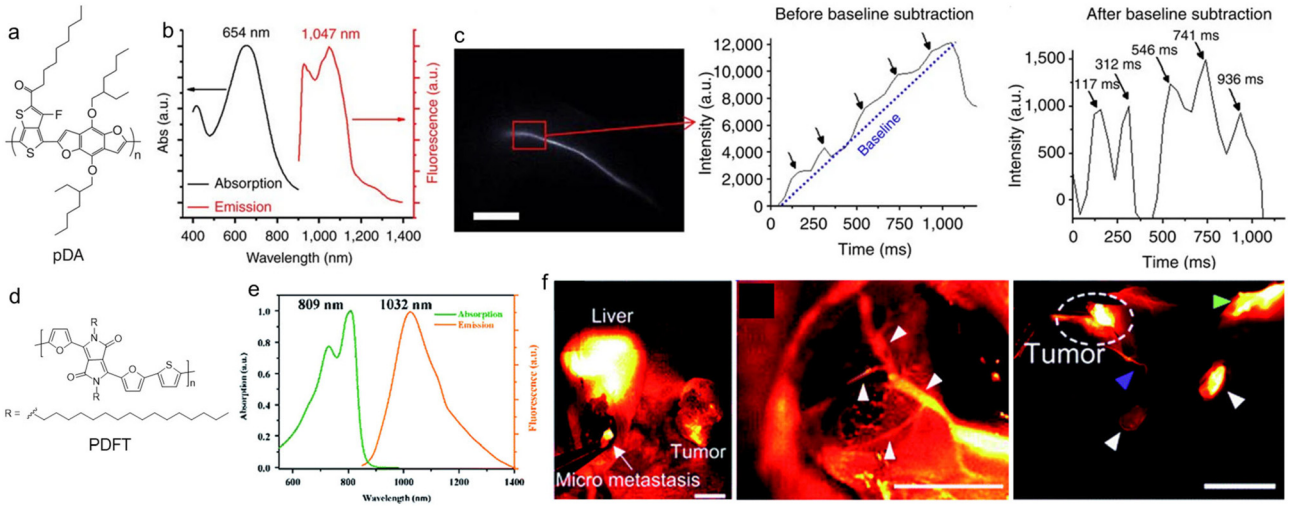

Fig. 2 a) Chemical structure of pDA. b) Absorption and PL spectra of pDA-PEG NPs. c) NIR-II fluorescence image of the mouse femoral artery and the humps featuring five cardiac cycles. Scale bar: 5 mm. Reproduced with permission Copyright©2014, Macmillan Publishers Limited.[66] d) Chemical structure of PDFT. e) Absorption and PL spectra of PDFT. f) Representative *in vivo* NIR-II fluorescence images of residual tumour identification, tumour vascular embolization and lymph node identification. The scale bars of the three images in (f) are, in sequence, 1.5 cm, 8 mm, and 8 mm. Reproduced with permission Copyright©2020, The Royal Society of Chemistry.[71]

shift of about 400 nm, so the emission wavelength could reach the NIR-II region of 1047 nm (Fig. 2b), and the fluorescence quantum yield was about 1.7%. First, the NIR-II imaging ability of pDA-PEG was verified at the cellular level. The amphiphilic polymer DSPE-PEG-NH_2 was coated on the surface and modified with cetuximab (Erbitux) antibodies, so that the polymer NPs were able to target the epidermal growth factor receptors on the cell membrane surface. Therefore, pDA-PEG NPs could be used for cell recognition and imaging. Subsequently, the NIR-II fluorescence of pDA-PEG NPs can also be used for *in vivo* vascular imaging and for testing real-time arterial blood flow in mice in a short exposure time (~20 ms). After intravenous injection, video-rate imaging was conducted with an ultrafast frame rate of 25.6 frames per second, which enabled clear observation of the blood flow in the femoral artery with an average blood velocity of 4.36 cm s^{-1}. Owing to the high resolution, the blood flow in small capillaries of less than 10 μm could still be traced. The high spatiotemporal resolution resulted in unambiguous imaging of the blood flow pattern in the cardiogram waveform of a living mouse (Fig. 2c), which was for the first time realized by NIR-II fluorescence imaging.

Diketopyrrolopyrrole (DPP) is a very good planar electron acceptor, and it has been widely used for building photovoltaic materials.[69,70] Because it can easily combine with different electron donors and shows good photostability and light harvesting ability, DPP-based structures have great potential for biomedical imaging applications. Cheng *et al.* designed a new type of SP (PDFT1032) based on DPP for NIR-II bioimaging and surgical navigation (Fig. 2d).[71] They designed and synthesized a narrow bandgap D–A copolymer, with thiophene (T) and 2,5-dihexadecyl-3,6-di(furan-2-yl) pyrrolo as the D unit and [3,4-*c*]pyrrole-1,4(2*H*,5*H*)-dione (DPP-2F) as the A unit to achieve NIR-II fluorescence. The maximal absorption/emission wavelength of PDFT1032 was 809/1032 nm, and the emission tail could extend to 1200 nm, showing a large Stokes shift of 233 nm and good photostability (Fig. 2e). Because the maximal allowable exposure intensity of the skin was stronger under NIR light irradiation beyond 800 nm, and the maximal absorption wavelength of PDFT1032 was 809 nm; this was more favourable for *in vivo* imaging using 808 nm light excitation than the ones with visible light excitation. PDFT1032 NPs were then used for *in vivo* vascular imaging, tumour imaging and tumour vascular imaging of mice to imply that their NIR-II imaging can be used for surgical navigation, and showed excellent sentinel lymph node (SLN) recognition imaging quality on normal mice and tumour-bearing mice (Fig. 2f).

Wu *et al.* reported the introduction of fluorine (F) into SPs to improve NIR-II fluorescence for quantitative brain tumour imaging.[72] Because of the large electronegativity and small atomic radius of the F atom, attaching a F substituent to the A group of the SP could help to reduce the molecular energy levels, enhancing the charge transfer and the molecular planarity.[73,74] They designed and synthesized two series of F-substituted SPs, in which benzodithiophene (BDT) was used as D and the triazole[4,5-*g*]-quinoxane (TQ) derivative as A (Fig. 3a). According to the position of the alkyl chain substituent on the TQ unit, the *m*-PBTQ and *p*-PBTQ SPs were divided into two series of polymers, and these polymers included six kinds of polymers with different F substitutions, named *m*-PBTQ, *m*-PBTQ2F, *m*-PBTQ4F and *p*-PBDQ, *p*-PBDQ2F, and *p*-PBDQ4F, respectively. It was found that the F atom could effectively adjust the optical properties of the SPs because it increased the planarization of the conjugated structure and reduced the entanglement of the polymer alkyl chain, and the emission wavelength would undergo a certain

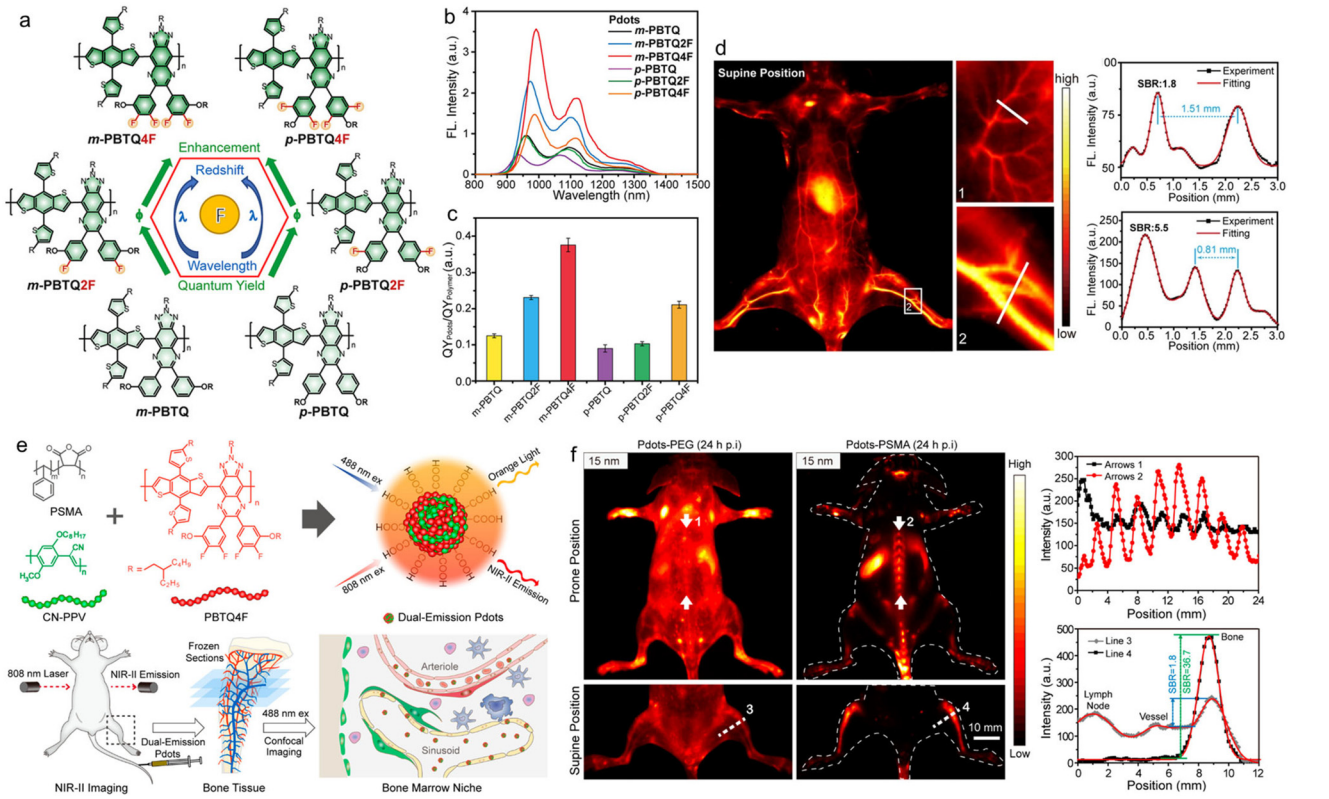

Fig. 3 a) Chemical structures of SPs with different fluorine substitutes and their influence on photophysical properties. b) PL spectra and c) fluorescence quantum yields of different SP NPs. d) *In vivo* NIR-II whole-body fluorescence imaging of mice and the cross-sectional fluorescence intensity profiles along white lines 1 and 2. Reproduced with permission Copyright©2020, Wiley-VCH GmbH.[72] e) Schematic illustration of the preparation of Pdots for imaging bone marrow retention. f) *In vivo* NIR-II fluorescence imaging of the mouse in prone and supine positions and the cross-sectional fluorescence intensity profiles along arrows 1 and 2. Reproduced with permission Copyright©2020, American Chemical Society.[75]

degree of red shift as the number of F atoms increased (Fig. 3b). The fluorescence quantum yield of *m*-PBTQ series Pdots was higher than that of *p*-PBTQ series Pdots, whether in organic solvent or in aqueous solution. Therefore, *m*-PBTQ4F Pdots possessed the best optical properties, and the fluorescence quantum yield of 3.2% was the highest among the NIR-II materials reported at that time (Fig. 3c). The increased brightness in F-substituted SPs might be derived from the suppression of quenching by the inter-chain interactions and non-emissive species. With the excitation of a low-intensity 808 nm laser (70 mW cm^{-2}), the whole-body imaging of a mouse in both supine and prone positions clearly showed the vascular structures (Fig. 3d). The through-scalp and through-skull brain imaging indicated that *m*-PBTQ4F Pdots were superior to the clinically approved imaging dye indocyanine green (ICG) for NIR-II imaging in terms of long imaging duration, high signal-to-noise ratio (SNR) and spatial resolution. Moreover, *m*-PBTQ4F Pdots were also applied to brain malignant tumour vascular imaging of mice, which could be used for real-time surgical navigation, as well as quantifying the cerebral vessels through the mouse scalp and skull.

Wu and coworkers further reported small polymer NPs for NIR-II fluorescence imaging of mouse bones, which implied that bones were important organs for the retention of small polymer NPs.[75] The small polymer NPs were composed of two equal weight mixtures, namely an orange light emission polymer (CN-PPV) with an emission wavelength of 590 nm and a fluorescence quantum yield of ~6% for *in vitro* microscopy imaging, and a SP (PBTQ4F) emitting in the NIR-II window with a maximal emission wavelength of about 1100 nm and a fluorescence quantum yield of ~1.9% for *in vivo* imaging (Fig. 3e). In order to endow the hydrophobic polymers with biocompatibility, they were wrapped with amphiphilic polymer poly(styrene-*co*-maleic anhydride) (PSMA) to obtain Pdots with different sizes: 15 nm, 25 nm, 50 nm, and 100 nm, respectively. After quantitative analysis of the fluorescence signal, it was shown that the fluorescence signal intensity of 15 nm Pdots in the bone distribution of mice was about 3.4 times higher than that of 50 nm Pdots, indicating that the particle size of 15 nm Pdots was easier to gather in the bones. They also verified the exact location of Pdots in bone tissue imaging, and a series of experimental studies suggested that Pdots were mainly absorbed by bone marrow sinusoidal vascular endothelial cells, and bones were important organs for the biodistribution of Pdots in addition to the liver, spleen and kidneys (Fig. 3f). This research would provide a new

direction for the treatment and diagnosis of bone-related diseases in the future.

The integration of conventional small molecular dyes and polymers would be a good strategy to take full advantage of their merits (*e.g.*, the high light absorption ability of conventional dyes and the good stability of polymers) and overcome their demerits (*e.g.*, the instability of conventional dyes and the low brightness of polymers).[76–78] Chan and coworkers designed and synthesized three types of polymethine-based SPs (Pttc-SeBTa-NIR1125/1270/1380) with narrow absorption and emission bands for NIR-IIb (1500–1700 nm) fluorescence imaging of whole-body blood vessels and the mouse brain.[79] They synthesized a SP with anti-ACQ properties because the rigid three-dimensional structure of the Pttc monomer and the steric hindrance of the SeBTa monomer were both conducive to preventing the ACQ effect. Then the derivative of fluorene on the polymer skeleton was modified with azide functional groups, which could react with the pigment molecules in the NIR region to obtain the target polymers Pttc-SeBTa-NIR1125/1270/1380 (Fig. 4a). The maximal absorption and emission of Pttc-SeBTa-NIR1125/1270/1380 were both located in the NIR-II window exceeding 1000 nm, which could enable better penetration depth and higher SNR. Through density functional theory (DFT) calculation and experiment verification, the dye molecules covalently attached to the polymer chain had better optical stability than the blend. In particular, the absorption/emission peaks of Pttc-SeBTa-NIR1380 were located at 1270/1380 nm. The fluorescence quantum yields of Pttc-SeBTa-NIR1125/1270/1380 were, in sequence, 0.18%, 0.09% and 0.05%, which were higher than those of most organic dyes in the similar response region. Then they compared the NIR-II imaging quality with four different types of long-pass filters (1020, 1100, 1250, and 1312 nm) with low-power 808 nm laser (5 mW cm^{-2}) excitation (Fig. 4b). Although the longer long-pass filter (*i.e.*, 1312 nm) resulted in lower fluorescence emission, the *in vivo* imaging displayed better spatial resolution and SBR for the reduced background interference in longer wavelength. The NIR-IIb emission of Pttc-SeBTa-NIR1380 enabled deeper penetration depth for the biological imaging of mouse brain blood vessels, tumours, and whole blood vessels (Fig. 4c and d).

Although the anti-ACQ strategy could avoid fluorescence quenching in the aggregate state, it can hardly improve the brightness. AIE has emerged as a favourable concept for boosting brightness, especially in the aggregate form. The fluorescence quantum yields of AIEgens can be very high, yet the light absorption ability is usually not high for the highly twisted molecular structure.[80,81] For example, tetraphenyl ethylene (TPE) is the most widely used building block of AIEgens, but the corresponding chromophores exhibit a relatively low absorption coefficient. As a result, the brightness of some AIEgens is not very high. The high brightness depends on two factors: one is the high absorption coefficient, and the other is the high fluorescence quantum yield.[80,82] Largely conjugated systems can help to improve the absorption coefficient of molecules but cause an ACQ problem in the aggregate state. However, twisted molecular frameworks are beneficial for improving the fluorescence quantum yield but the conjugation is reduced.[83] Accordingly, the balance of the absorption coefficient and fluorescence quantum yield might be a good solution. Tang *et al.* reported high-brightness NIR-II SP NPs for biomedical imaging.[84] They designed and synthesized a high-brightness D–A polymer (pNIR-4) that combined the advantages of the high absorption coefficient of ACQ molecules and the high fluorescence quantum yield of AIE molecules (Fig. 5a). It was made of triphenylamine (TPA) and thiophene as the donor, and benzo[1,2-*c*:4,5-*c*′]bis([1,2,5]thiadiazole) (BBTD) as the

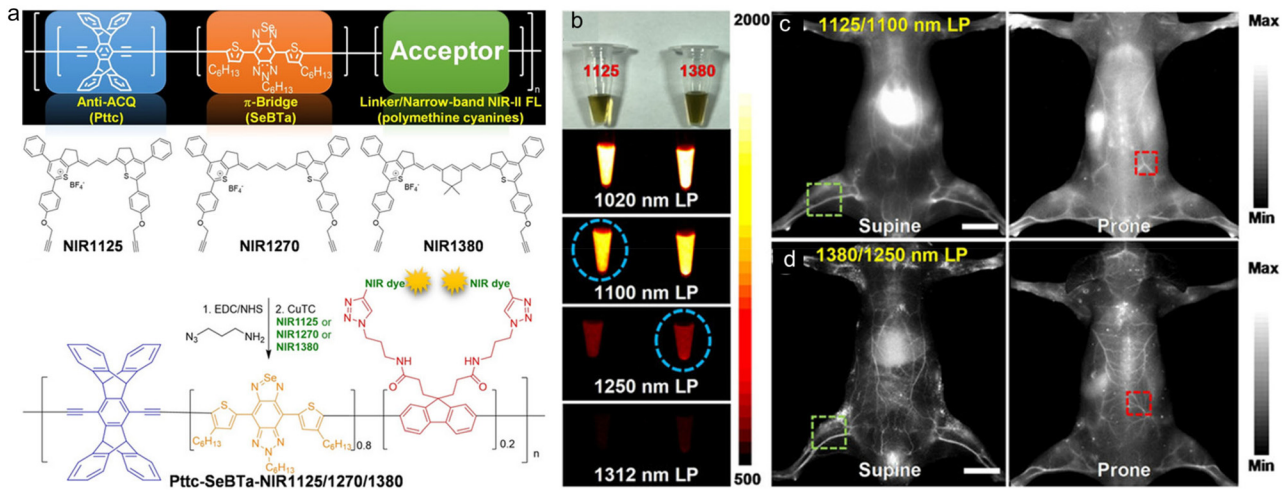

Fig. 4 a) Molecular design and chemical structures of polymethine dye-based SPs (NIR1125, NIR1270 and NIR1380). b) Photographs of Pttc-SeBTa-NIR1125 (left) and Pttc-SeBTa-NIR1380 (right) Pdot solution, and fluorescence images under 808 nm laser excitation with different long-pass filters as indicated. *In vivo* whole-body imaging of the living mice intravenously injected with c) Pttc-SeBTa-NIR1125 Pdots and d) Pttc-SeBTa-NIR1380 Pdots in supine and prone. Scale bars: 10 mm. Reproduced with permission Copyright©2020, Wiley-VCH GmbH.[79]

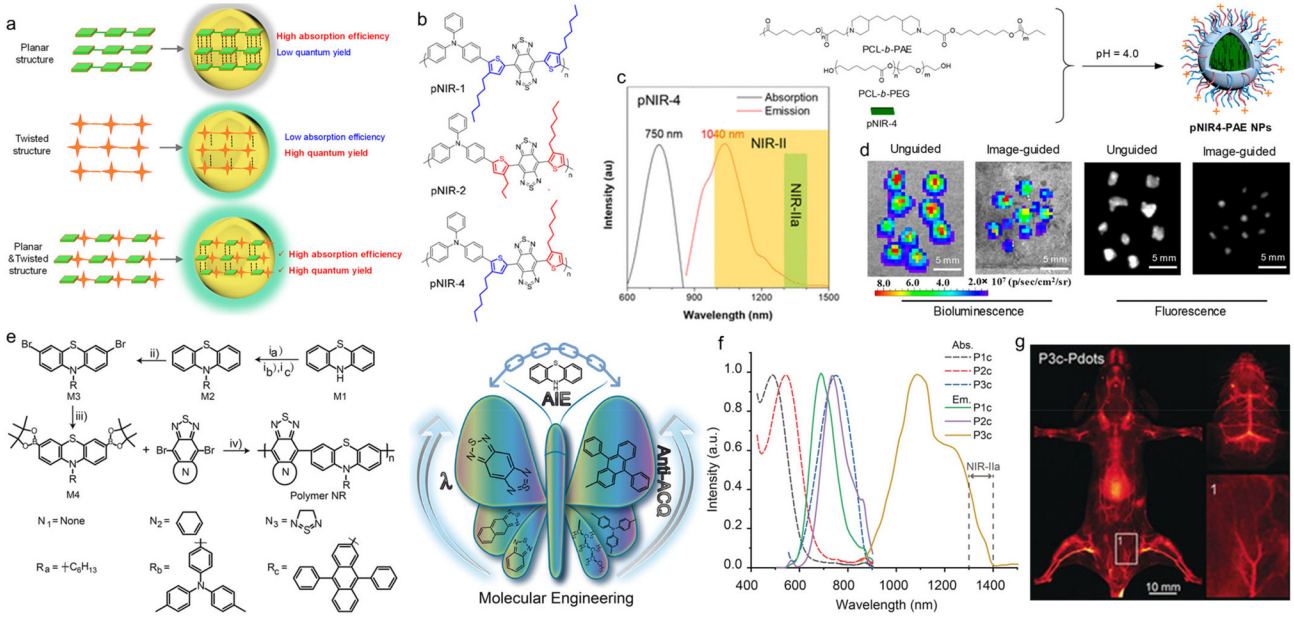

Fig. 5 a) Schematic illustration of the molecules with planar, twisted and planar plus twisted structures. b) Chemical structures of different SPs. c) Absorption and PL spectra of pNIR-4 NPs. d) Bioluminescence and NIR-IIa fluorescence imaging of resected nodules of unguided and pNIR4-PAE NP-guided groups. Reproduced with permission Copyright©2020, American Chemical Society.[84] e) Chemical structures of AIE SPs based on phenothiazine and the properties. f) Absorption and PL spectra of P1c, P2c, and P3c Pdots. g) *In vivo* NIR-II fluorescence images of the mouse hindlimb vasculature intravenously injected with P3a Pdots. Reproduced with permission Copyright©2019, Wiley-VCH Verlag GmbH & Co. KGaA, Weinheim.[85]

acceptor. They first synthesized a series of polymer derivatives with similar structures (Fig. 5b). By comparing the optical properties with DFT, the donor and the position of the alkyl chain substituent on the thiophene ring, they obtained the following conclusions: (1) by comparing the dihedral angles, it was found that the adjacent loop of the alkyl chain in BBTD improved the structural twist of T–BBTD–T, making T–BBTD–T a planar structure in the *meta* position, (2) TPA had a stronger electron feeding effect than the popularly used TPE, which made the absorption and emission wavelengths redshift. The polymer pNIR-4 adopted the structure that one alkyl chain was adjacent to the BBTD and the other alkyl chain was located on the other side. The absorption and emission wavelengths were 709 nm and 1010 nm, respectively, with a fluorescence quantum yield of 2.24% and a quantum efficiency (QE) of 128. Then a pH-responsive block copolymer of poly(ε-caprolactone) and poly(β-amino ester) (PCL-*b*-PAE) was used to increase the biological solubility (Fig. 5c). In addition, under acidic conditions, PAE became positively charged to increase the uptake of tumour cells and the aggregation of NPs, enhancing the imaging performance of pNIR-4 at the tumour site, and could be used for precise surgical navigation during surgery. The NIR-II fluorescence imaging-guided surgery in peritoneal carcinomatosis-bearing mice helped to excise the sub-millimeter tumour nodules in a very sensitive way (Fig. 5d).

Wu *et al.* reported a D–A structure SP for cerebral vascular imaging in mice.[85] They designed the molecule from two aspects to achieve NIR-IIa (1300–1400 nm) fluorescence emission. On the one hand, to improve the AIE properties of the SP, phenothiazine (PTZ) was selected as the donor since the middle six-membered ring had a nonplanar structure with a dihedral angle of 153° for the presence of a sulfur atom and nitrogen atom.[86] Additionally, the PTZ molecule had multiple reaction sites and excellent reactivity suitable for polymerization. On the other hand, due to the different mechanisms of AIE and ACQ properties, AIE and ACQ phenomena can exist in one polymer at the same time, while ACQ would weaken the fluorescence intensity of molecules. Therefore, the anti-ACQ effect could be achieved by adding alkyl chains to the nitrogen atom of PTZ by increasing the steric hindrance. Different side groups and three different A units were chosen to synthesize nine kinds of SPs (Fig. 5e). By comparing the absorption, emission and AIE properties of these polymers in different solutions and different aggregate states, they finally selected P3c for cerebral vascular imaging in mice. The absorption peak of P3c in THF solution was about 740 nm, the emission range was 1100–1400 nm, and the fluorescence quantum yield in aqueous solution was 1.7%, which suggested that P3c exhibited good NIR-II imaging properties (Fig. 5f). The cerebral vascular system of the mice was imaged with the fluorescence emission of P3c in the NIR-IIa window beyond 1300 nm. Because of the excellent emission performance of P3c, the cerebral vessels of the mice could be clearly seen without craniotomy (Fig. 5g).

Multimodality imaging strategy can be used to overcome the shortcomings of the single imaging mode and improve

the diagnostic accuracy.[87,88] Because the attenuation of ultrasound in the body is far less than light, PA imaging holds great advantages of good spatial resolution and deep tissue penetration depth.[89–91] Therefore, the integration of fluorescence and PA would provide comprehensive information.[92,93] Liu *et al.* reported NIR-II fluorescence and PA dual-mode imaging with SPs for vascular imaging and brain micro tumour imaging in mice.[94] They first designed and synthesized a low-bandgap SP with a good ICT effect, low bandgap, high extinction coefficient and good light stability that could be used for both NIR-II fluorescence imaging and PA imaging. The polymer poly(benzodithiophene (BDT)-*alt* thiadiazolobenzotriazole (TBZ)) (PBT) was composed of an electron-donating BDT unit and electron-donating TBZ (Fig. 6a). PBT exhibited maximal absorption at ~1064 nm in the NIR-II region with an excitation coefficient of 22.1 L g^{-1}, and maximal emission at 1156 nm with a tail extending to 1650 nm, and the fluorescence quantum yield was about 0.1% (Fig. 6b and c). The NIR-II fluorescence imaging of PBT NPs in mice helped to clearly distinguish the microvessels with a diameter of about 710 nm and at a signal-to-background ratio (SBR) of 2.0. The NPs could be retained *in vivo* for more than 6 h, which held the potential of long-term angiography (Fig. 6d). Then it was used to track the fast-flowing arterial blood flow, and the blood flow rate was determined to be 238.6 μM s^{-1}, corresponding to a volume blood flow of 5.67 × 10^{-4} μL min^{-1}. Focused ultrasound (FUS) combined with microbubbles could temporarily open the blood–brain barrier (BBB), which was conducive to the PA imaging of small tumours in the early stage by PBT NPs, and the large tumours in the later stage could also be visualized by PA imaging through the enhanced permeation and retention (EPR) effect (Fig. 6e). The NIR-II fluorescence and PA dual-mode imaging in one polymer was demonstrated for the first time, which provided good application prospects and development potential for such molecules.

3. NIR-II SPs for *in vivo* disease diagnostics and therapy applications

Organic/polymer NIR-II emitters hold great potential for biomedical applications. However, the organic NIR-II probes reported so far usually suffer from the following two problems: i) the effective NIR-II brightness (emitting photons at wavelengths greater than 1000 nm) is low, and ii) the laser power density required to perform photothermal treatment is much higher than the maximum permissible exposure (MPE). Therefore, the development of new NIR-II fluorescent probes with higher effective NIR-II brightness and the ability to perform PTT at safe laser energy densities (below or equal to MPE) is still an urgent problem to be solved. Liu *et al.* developed a novel SP nanoprobe as a treatment reagent (L1057 NPs).[95] Unlike the strategy of designing NIR-II fluorescent materials using strong electron-deficient units (*e.g.*, BBTD) as the acceptors, which is often used in the literature, this work took advantage of the long conjugation length of SPs to achieve absorption and emission redshifts by using weak electron-deficient A units (Fig. 7a). The extinction coefficient of L1057 NPs at 980 nm was 18 L g^{-1} cm^{-1}, which was higher than most reported in the literature (2–10 L g^{-1} cm^{-1}). Meanwhile, the vast majority of their emission spectra were within the NIR-II region (the emission peak at 1057 nm) and possessed high quantum yields (1.25%) in the NIR-II region (Fig. 7b and c). It should be noted that the effective NIR-II fluorescence brightness is determined by the extinction coefficient at the excitation wavelength, the fluorescence quantum yield, and the ratio of the emission spectrum to the full spectrum in the NIR-II region. Subsequently, the NIR-II fluorescence imaging performance was verified by *in vivo* NIR-II macroscopy and microscopy imaging. In the whole-body angiography in living mice, blood vessels of approximately 200 μm in diameter could be clearly displayed. In cerebral vascular microscopy, even the cerebral vessels of 1.9 μm could be clearly displayed with a high SNR. In craniotomized mice, the cerebral vasculature was detected

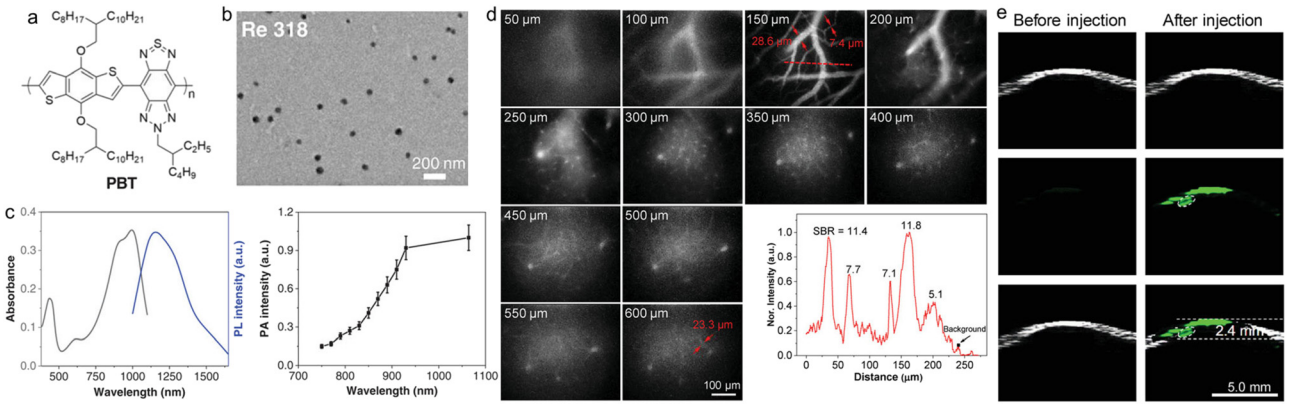

Fig. 6 a) Chemical structure of PBT. b) TEM image of PBT NPs. c) Absorption, PL spectra and PA profile of PBT NPs. d) *In vivo* NIR-II microscopy fluorescence imaging of cerebral vasculatures in different depths. e) *In vivo* PA imaging of the deep orthotopic brain tumour in a mouse. Reproduced with permission Copyright©2019, WILEY-VCH Verlag GmbH & Co. KGaA, Weinheim.[94]

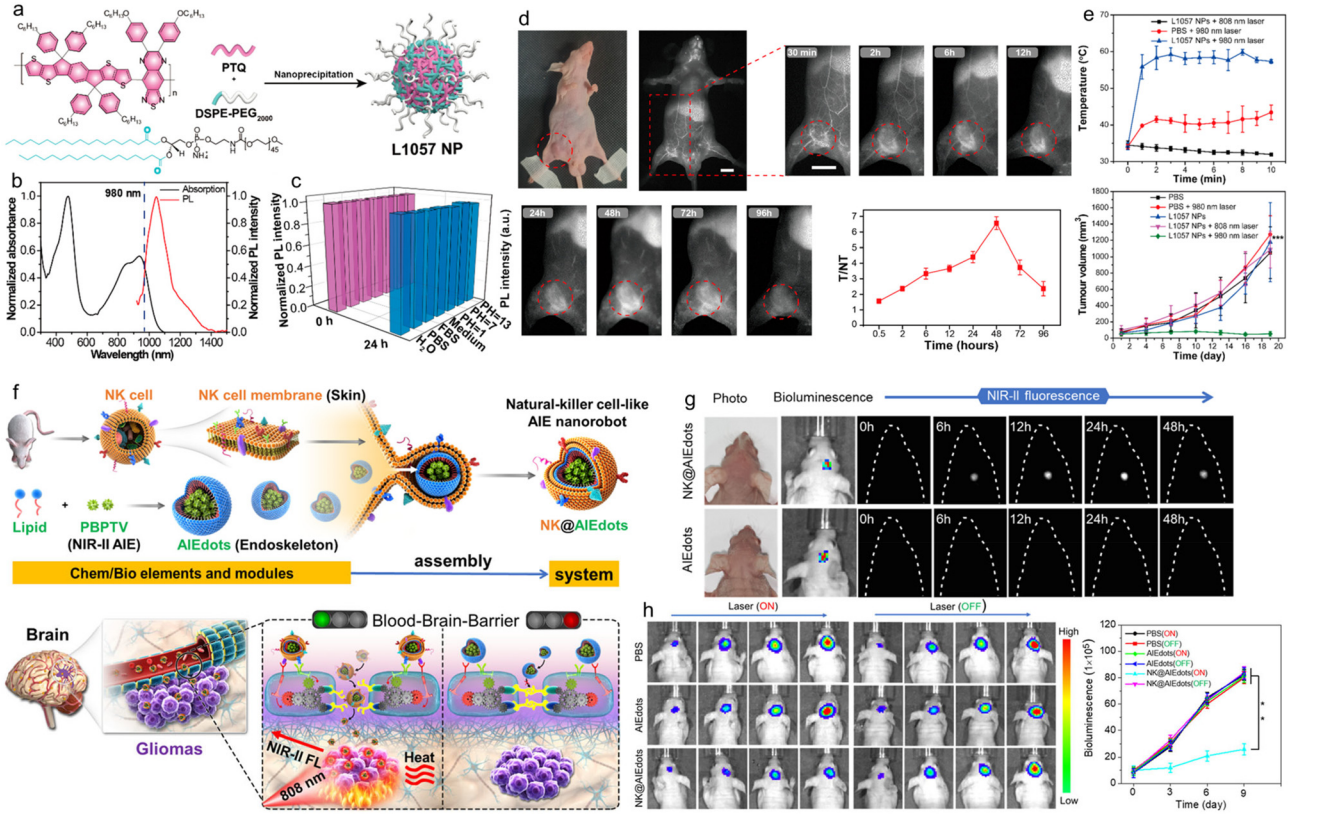

Fig. 7 a) Chemical structure of PTQ and schematic illustration of the preparation of L1057 NPs. b) Absorption and PL spectra of L1057 NPs. c) Fluorescence stability of L1057 NPs under various conditions. d) *In vivo* NIR-II fluorescence imaging of 4T1-tumour-bearing nude mice at different time points after treating with L1057 NPs. Scale bars: 1 cm. e) Photothermal effect and tumour volume of 4T1-tumour bearing mice under 808 nm (0.33 W cm^{-2}) or 980 nm (0.72 W cm^{-2}) laser irradiation. Reproduced with permission Copyright©2020, American Chemical Society.[95] f) Schematic illustration of NK-cell-mimic AIE NPs (NK@AIEdots) for brain tumour targeted light-up and inhibition. g) Noninvasive through intact scalp and skull *in vivo* NIR-II fluorescence imaging of the mouse brain under 808 nm laser excitation after treating with AIEdots (PBPTV) and NK@AIEdots (PBPTV) for different times. h) *In vivo* bioluminescence imaging and corresponding intensity of orthotopic glioma at different time points after PTT. Reproduced with permission Copyright©2020, American Chemical Society.[104]

to a depth of 900 μm with 980 nm light excitation. In a mouse model of transplantation tumour, L1057 NPs were efficiently aggregated at the tumour location by tail vein injection, providing good tracing of the tumour (Fig. 7d). According to ANSI Z136.1-2007, American National Standard for Safe Use of Lasers, the MPE of skin is 0.33 W cm^{-2} for 808 nm, 0.4 W cm^{-2} for 850 nm, 0.72 W cm^{-2} for 980 nm, and even 1.0 W cm^{-2} for 1064 nm.[96–98] At present, the majority of organic NIR-II fluorescent probes for PTT are using an 808 nm laser, which, together with the low extinction coefficient, leads to a much higher laser power density than MPE, resulting in limited prospects for clinical applications. The new L1057 NPs not only had a high extinction coefficient and photothermal conversion efficiency (38%), but also cleverly used 980 nm wavelength as the excitation light for PTT of tumour-bearing mice, demonstrating a superior and safer treatment effect compared to the 808 nm laser (Fig. 7e). The NPs and their derivatives in this work might have a profound impact on clinical medicine, for example, they could be applied to various disease models, such as surgical navigation of atherosclerosis.

Gliomas are health-destroying killers that can interfere with the normal physiological activity of the central nervous system.[99,100] Surgery is the most common treatment for gliomas, but most gliomas would infiltrate into normal brain tissue, making it difficult to distinguish tumour margins. In addition, the presence of the BBB also creates a barrier for contrast agents or drugs to enter the brain.[101,102] Natural killer cells (NK cells) are a type of immune cell in the body that stimulates an immune response to directly kill targeted cancer cells.[103] Tang *et al.* used NK cell membranes wrapped with an AIE SP with NIR-II fluorescence properties to fabricate NK cell bionic AIE nanorobots and applied them to the diagnosis and treatment of glioma (Fig. 7f).[104] First, the NIR-II AIE-active polymer PBPTV was prepared using the regioregular bispyridal[2,1,3]thiadiazole (BPT) unit as the acceptor and the alkyl-substituted (*E*)-2-(2-(thiophen-2-yl) vinyl)-thiophene (TVT) unit as the donor. Under 808 nm laser irradiation, the polymer PBPTV could emit very bright fluorescence with a quantum yield of 8.6%, which was four times stronger than those of previously reported NIR-II polymers. Then NK@AIE dots were prepared by encapsulating the cell membrane of NK cells onto the PBPTV

nano-aggregate material backbone (AIE dots) by bionic virus outgrowth. The function of NK cells was associated with multiple antibodies on their cell membrane surface, so NK@AIE dots could interact with the cells on the BBB to open it, modulate the tight junctions (TJs) between the epidermal cells of the BBB, and lead to an increase in the cell gap to cross the BBB. At the same time, the antigen specificity of the NK cell membrane was used to recognize antibodies of cancer cells and effectively stay inside glioma cells after crossing the BBB to achieve high SNR brain tumour NIR-II fluorescence imaging. In addition, PBPTV had strong NIR absorption and could be used for PTT. The photothermal conversion efficiency of NK@AIE dots was 45.3%. Its good *in vivo* glioma-targeted photothermal treatment effect was further confirmed by an *in situ* glioma model (Fig. 7g and h). This work improved the ability of NPs to penetrate the BBB by using the NK cell membrane to stimulate immune response and provided an efficient drug delivery tool for brain diseases.

PTT is a safe cancer treatment strategy that uses photothermal conversion agents (PCAs) to convert light energy into heat to ablate cancer cells. However, high-temperature PTT inevitably damages the surrounding healthy tissues and may lead to inflammatory diseases due to the difficulty in blocking heat diffusion.[105,106] In addition, the high-temperature thermal ablation can cause systemic immune response with harmful adverse effects in cancer treatment. Low-temperature PTT has become an emerging treatment strategy because it could ablate tumours in the low-temperature range (below 45 °C) and avoid damage to normal cells.[107] However, the ablation effect at relatively low temperatures is insufficient due to the upregulation of the expression of heat shock proteins (HSPs), which repair heat-damaged cells and lead to thermal tolerance of tumour cells to laser irradiation.[108] Therefore, it is imperative to investigate new HSP silencing strategies in low-temperature PTT. Recently, Gong *et al.* synthesized a carbon monoxide (CO)-storage polymer mPEG(CO) using dodecacarbonyltriiron and mercapto polyethylene glycol ($mPEG_{2000}$-SH), which was further embedded with NIR-II AIE polymer PBPTV to form chemical excitation to trigger AIE nanobomb PBPTV@mPEG(CO) (Fig. 8a).[109] This smart nanobomb had a broad absorption in 550–850 nm with a maximum absorption wavelength of 810 nm. Under the excitation of an 808 nm laser, the nanobomb showed strong fluorescence centred at 970 nm, which could extend to the NIR-II region (Fig. 8b). After intratumoural injection of the nanobomb into tumour-bearing mice, the tumour was irradiated with the 808 nm laser and the temperature was maintained at ~43 °C (Fig. 8c and d). Since in the tumour microenvironment, the over-secreted H_2O_2 diffused to the nanobombs through the Fenton-like reaction catalyzed by FeCO and preferentially decomposed into ˙OH radicals, the strongly oxidized ˙OH radicals further oxidized and competed with the Fe centre for coordination, leading to the release of CO from the Fe centre. And then the gradually released CO could effectively inhibit the elevated expression of HSPs during cryo PTT (43 °C), disrupt the tumour thermal resistance and induce apoptosis, showing a good tumour suppression effect by combining CO treatment and low-temperature PTT (Fig. 8e). After meeting H_2O_2, the self-assembled smart nanobomb released CO to cancer cells, which could improve the efficiency of tumour treatment.

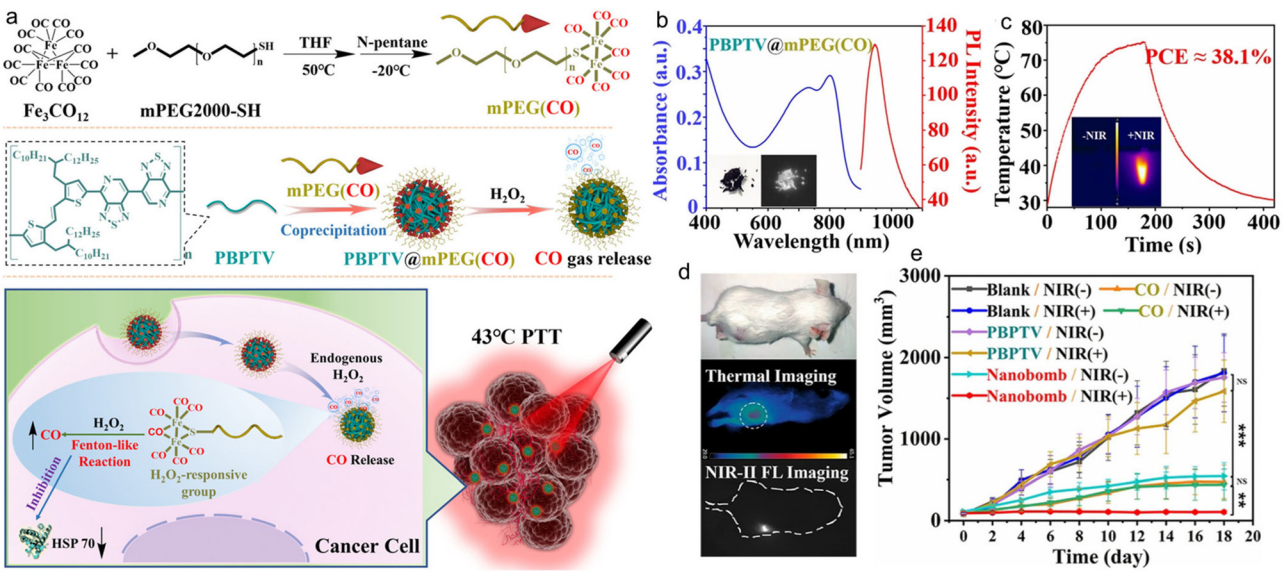

Fig. 8 a) Schematic illustration of the nanobomb consisting of mPEG(CO) and PBPTV for low-temperature PTT. b) Absorption and PL spectra of the nanobomb solution. c) Photothermal properties of the nanobomb solution under 808 nm laser irradiation. d) Photothermal treatment and NIR-II fluorescence imaging of tumour-bearing mice. e) The tumour volume of the tumour-bearing mice after PTT. Reproduced with permission Copyright©2022, Wiley-VCH GmbH.[109]

The overactive immune response caused by excessive temperatures during PTT may exacerbate skin burns, which lead to permanent tissue damage and tumour regeneration.[110] Therefore, the search for an anticancer balance between pathological and protective immune responses is urgently needed in advanced phototherapeutics. Hydrogen sulfide (H_2S), a typical biogas transmitter, has unique cytoprotective effects, upregulating endogenous antioxidant systems and significantly neutralizing hyperactive inflammation.[111,112] However, the unstable chemical nature of H_2S hinders its direct application in PTT immunomodulation. Due to the thiol-rich microenvironment at tumour sites, polysulfide donors may have tumour-specific sulfide therapeutic and anti-inflammatory functions that reduce side effects on normal tissues. With this in mind, Dai *et al.* constructed a multifunctional H_2S nanomodulator by combining an amphiphilic SP with a polysulfide-based H_2S donor, which could down-regulate the over-activated photothermal immune effect in combined cancer PTT while accelerating the recovery of photothermally burned skin tissue (Fig. 9a).[113] The nanoimmunomodulator was designed by integrating an amphiphilic conjugated polymer (CP-PEG) and a polysulfide structured H_2S donor (Pry-Ps). The synthesized CP-PEG exhibited an absorption peak in the NIR region (700–1100 nm, λ_{max} = 900 nm) and exhibited broad NIR-II emission (900–1400 nm, λ_{max} = 1140 nm) under 808 nm light excitation, indicating that Pry-Ps@CP-PEG could be used as a NIR-II fluorescence imaging probe. The *in vivo* NIR-II imaging of tumour-bearing mice helped to light up the tumour site (Fig. 9b). Meanwhile, Pry-Ps@CP-PEG had a good photothermal effect with a photothermal conversion efficiency of up to 43.7%. In addition, glutathione (GSH), a major source of cytosolic thiols enriched in tumours, can trigger the release of H_2S from PryPs donors and thereby induces mitochondrial dysfunction and anti-inflammatory potential. The combination treatment of H_2S and PTT enabled Pry-Ps@CP-PEG to simultaneously possess anti-tumour properties and also alleviate the pro-inflammatory symptoms induced by photothermal treatment (Fig. 9c). Finally, this strategy of gas-regulated PTT was verified in a 4T1 hormonal mouse model to significantly inhibit tumour growth and limit the amounts of PTT-induced pro-inflammatory tumour necrosis factor-α (TNF-α), interleukin-6 (IL-6) and interleukin-1β (IL-1β) cytokines (Fig. 9d). In addition, this regulated inflammation could also accelerate the promotion of PTT-induced wound healing. By regulating the endogenous gas H_2S, it would play a certain role in cell protection and had strong influence on tumour treatment, so it could strengthen the treatment efficacy.

Bioimaging agents are often used to label specific drugs or drug-loaded NPs. However, the drug labelling process may alter the physicochemical properties of the original drug, which leads to significant differences between the real drug metabolism and imaging results.[114,115] It is important to develop drug delivery systems that can track the distribution and metabolism of drugs in real time and provide real-time feedback on the effectiveness of therapy. With this in mind, Xiao *et al.* designed a tandem NIR-II fluorophore with an ROS-responsive biodegradable NIR-II polymer.[116] As shown in Fig. 10a, the polymer main chain contained H_2O_2-sensitive sulfur condensation ketone bonds with negatively charged carboxylic acids in the side links, which were modified with a highly efficient cationic platinum (Pt) DNA embedding agent,

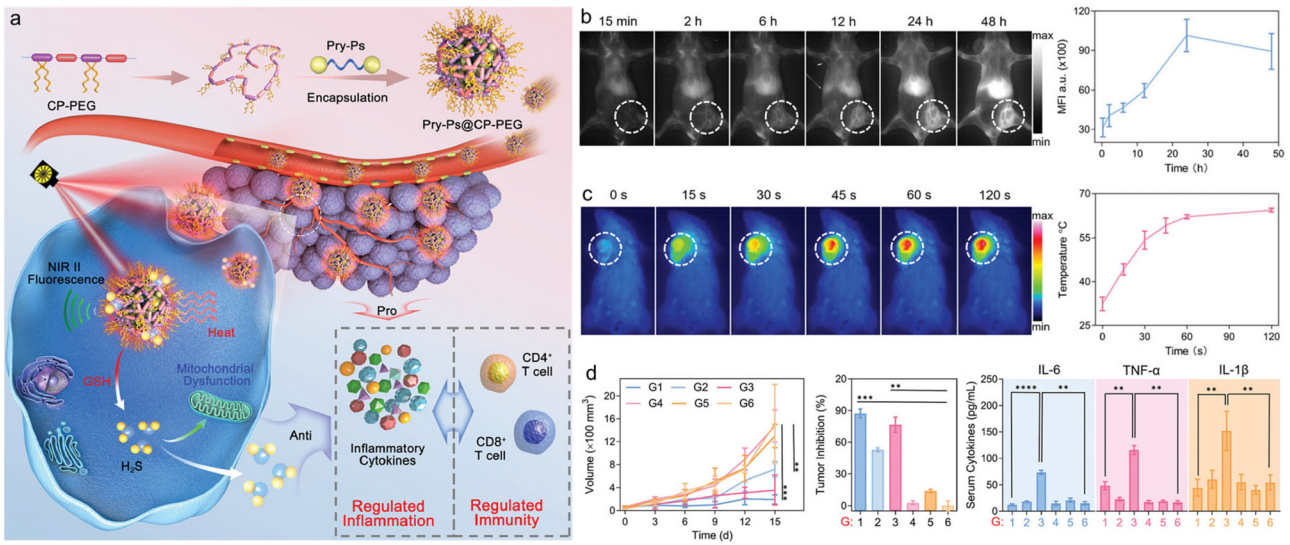

Fig. 9 a) Schematic illustration of the NIR-II fluorescence traced inflammation nanoregulator for dual-functional H_2S and PTT with modulated immunogenicity. b) *In vivo* NIR-II fluorescence imaging and corresponding fluorescence intensity of 4T1-tumour-bearing mice at different time points after intravenous injection of Pry-Ps@CP-PEG. c) The temperature changes during PTT. d) The tumour growth and proinflammation cytokine levels (IL-6, TNF-α, and IL-1β) in sera of tumour-bearing mice after PTT. Reproduced with permission Copyright©2021, Wiley-VCH GmbH.[113]

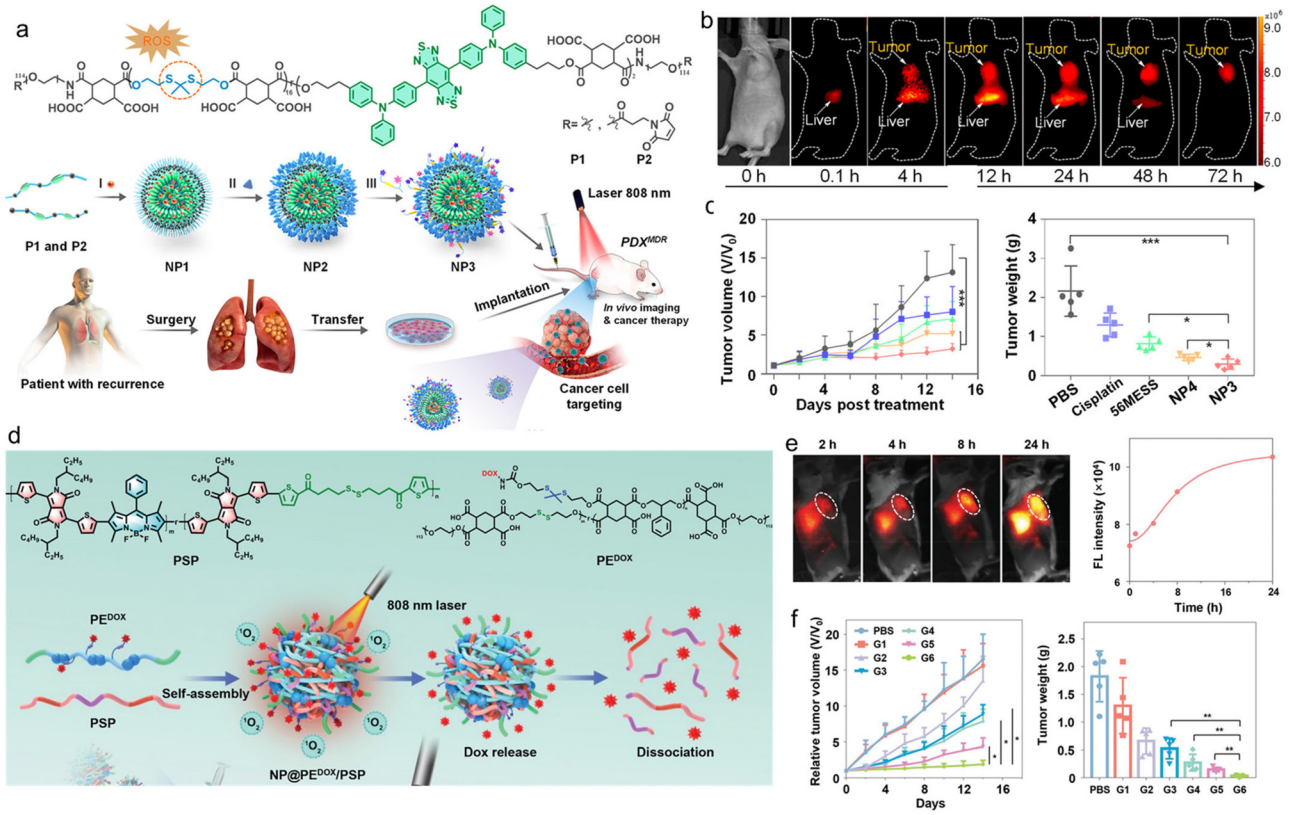

Fig. 10 a) Schematic illustration of the ROS-responsive biodegradable NIR-II SP for drug delivery and bioimaging. b) *In vivo* NIR-II fluorescence imaging of tumour-bearing mice. c) Relative tumour volume and tumour weight of the tumour-bearing mice after different treatments. Reproduced with permission Copyright©2021, American Chemical Society.[116] d) Schematic illustration of the self-sacrificially degradable NIR-II theranostic NP@PE^{DOX}/PSP for photodynamic immunotherapy and PACT. e) *In vivo* NIR-II fluorescence imaging and corresponding intensity of the mice at different time points after injecting NP@PE^{DOX}/PSP. f) Relative tumour volume and tumour weight during the treatments. Reproduced with permission Copyright©2022, Wiley-VCH GmbH.[117]

56MESS, to form NPs (NP1). Then, a sulfur-containing peptide (HS-RGD), which could be used to target αvβ3 integrins upregulated in cancer cells, and a cleavable short peptide probe (5′-FAM-DEVD-dabcyl) for cysteine as partase (caspase-3) were introduced into NP1 to form NPs (NP2 and NP3). The resulting NP3 had an emission peak at 1000 nm under 808 nm light excitation, which could be used for NIR-II fluorescence imaging to help to understand the fate of NPs *in vivo*. In addition, NP3 had superior biodegradability and tumour targeting ability, which could enter cancer cells and penetrate 3D tumour spheres (Fig. 10b). And its potency was approximately 4–1000 and 1.5–10 times higher than that of cisplatin and 56MESS, respectively. Subsequently, NP3 were injected intravenously into mice with a patient-derived tumour model of multidrug-resistant lung cancer (PDXMDR) (Fig. 10c). After injection, NP3 accumulated at the tumour site through blood circulation. This led to apoptosis and cystathione-3 production, cleaving the DEVD peptide and turning on the fluorescence of 5′-FAM (λ_{em} = 488 nm, λ_{em} = 520 nm) for apoptosis imaging. Finally, label-free laser desorption/ionization mass spectrometry imaging was used to visualize the *in situ* release of 56MESS in tumour tissues of mice treated with NPs by quantitative *in situ* monitoring of the signal intensity of the intrinsic mass spectrometry peaks of the drug.

Xiao *et al.* designed and prepared a self-sacrificing biodegradable pseudo-SP (PSP) for NIR-II fluorescence bioimaging, photodynamic immunotherapy, and photoactivated chemotherapy (PACT).[117] The PSP consisted of the monomer 2,5-bis(2-ethylhexyl)-3,6-bis(5-(trimethylstannyl) thiophen-2-yl)-2,5-dihydropyrrolo-[3,4-*c*]pyrrole-1,4-dione (defined as M1) with strong electron-withdrawing properties, the monomer 2,6-diiodo-4,4-difluoro-1,3,5,7-tetramethyl-8-phenyl-4-bora-3*a*,4*a*-diaza-*s*-indacene (defined as M2), and the reduction-sensitive monomer dithiobis(ethane-2,1-diyl) bis(5-bromothiophene-2-carboxylate) (defined as M3). Subsequently, the PSP was co-assembled with an amphiphilic polyester with disulfide bonds on the main chain and chemotherapeutic drug doxorubicin (DOX) on the side chain *via* ROS-responsive thione bonds (denoted as PE^{DOX}) to form biodegradable NIR-II therapeutic NPs (NP@PE^{DOX}/PSP) (Fig. 10d). Under 808 nm laser irradiation, NP@PE^{DOX}/PSP could efficiently generate ROS for photodynamic immunotherapy and display intense NIR-II fluorescence (Fig. 10e). Meanwhile, ROS could disrupt the thioketone bond in PE^{DOX}, leading to the rapid release of DOX for PACT.

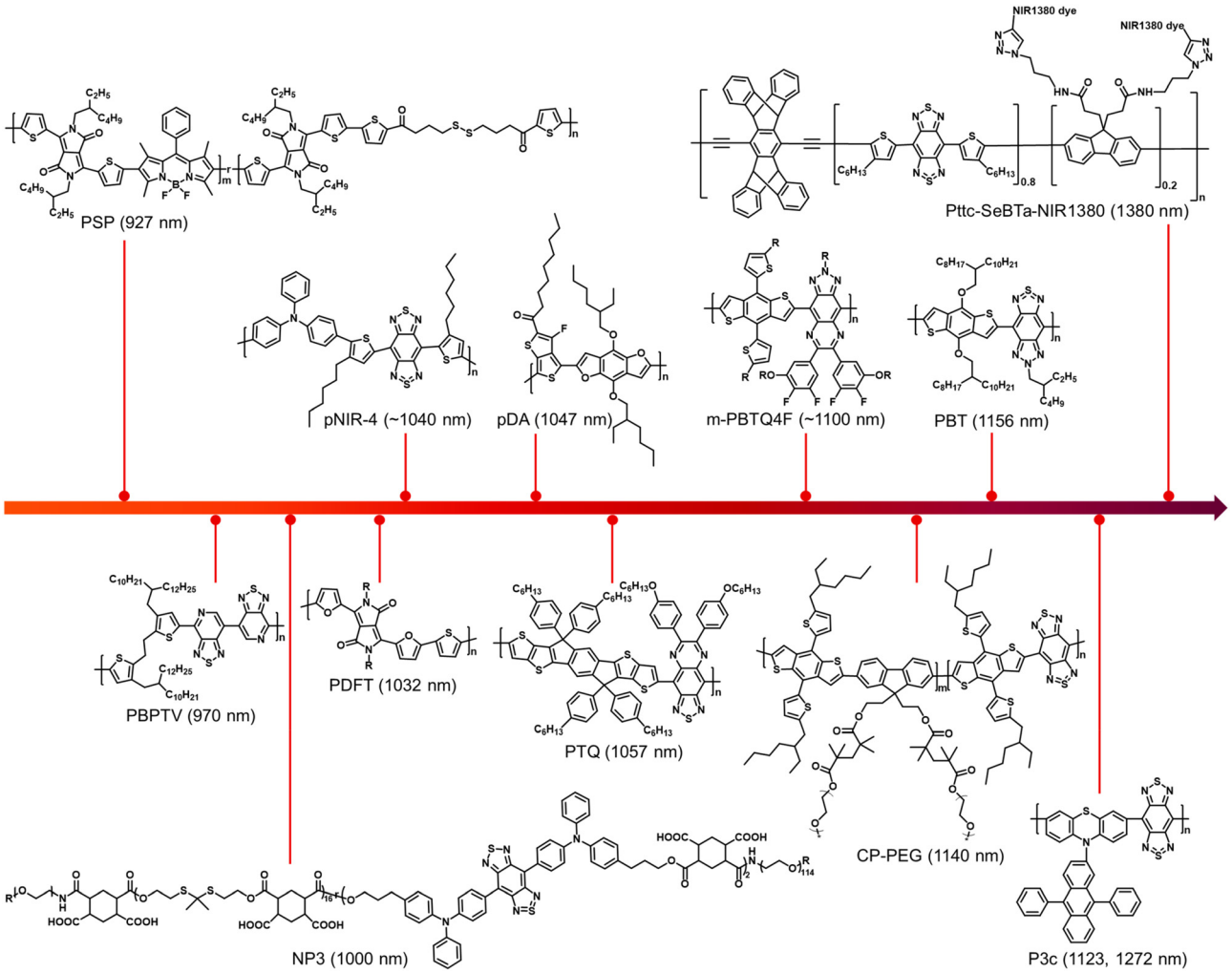

Chart 1 A summary of the chemical structures and emission wavelengths of the NIR-II SPs discussed in this review.

In addition, both PE^{DOX} and PSP were sacrificially degraded by intracellular GSH, leading to the dissociation of $NP@PE^{DOX}$/PSP. Finally, the superior tumour growth inhibitory properties of $NP@PE^{DOX}$/PSP were validated in 4T1 tumour-bearing mouse models with an adequate safety profile (Fig. 10f). This research demonstrated the precise imaging and chemotherapy of cancer, which would provide insight for future clinical applications.

4. Conclusions and outlook

Over the last decade, continuous attention has been focused on the development of NIR-II fluorescence SPs for biomedical applications. Much progress has been made in tuning the structure and manipulating the properties of SPs, as well as exploring various applications. This review highlights the recent achievements of SPs with NIR-II fluorescence emission for precise diagnostics and theranostics. A summary of the chemical structures and emission wavelengths of the NIR-II SPs discussed in this review is presented in Chart 1. The typical high-performance NIR-II SPs are introduced, and the strategies including anti-ACQ and AIE for realizing highly bright fluorescence are highlighted. NIR-II fluorescence SPs with other functions such as PA imaging, PTT, and PDT for disease theranostics are discussed. The emerging biomedical applications of NIR-II SPs such as *in vivo* high-resolution angiography, brain imaging, phototheranostic integration of fluorescence diagnostics and PTT, and immunotherapy are also presented. Although promising, NIR-II fluorescence SPs still face some obstacles for real applications. 1. Biocompatibility is one of the most important considerations for clinical use. Therefore, it is necessary to comprehensively evaluate the biocompatibility of several high-performing SPs to promote the clinical translation. 2. The biomedical applications are mainly focusing on tumours, and more attention should be paid to applications in other important diseases such as cardiovascular diseases and neuron diseases in the future. 3. The brightness of NIR-II SPs is not high enough as compared with small molecular emitters. Further effort should be directed to increase the fluorescence brightness. For example, the removal of impurities and the AIE strategy might be useful. 4. The emission wavelengths of

most NIR-II SPs are in the range of 1000–1200 nm. The bandgaps of SPs could be very small, but longer-wavelength NIR-II SPs are very rare. New strategies to ensure both the brightness and increased maximal emission to the NIR-IIa and even NIR-IIb window would be important for this field. This review will provide guidance for designing high-performance NIR-II SPs to realize maximized effectiveness of various bio-applications, and it will also provide comprehensive understanding about the chemical structure–photophysical property–biomedical application relationships of organic phototheranostic materials.

Author contributions

Xiaoying Kang: conceptualization, writing – original draft, writing – review & editing. Shuai Yin: writing – original draft, writing – review & editing. Jianwen Song: writing – review & editing. Yuan Zhang: writing – review & editing. Ji Qi: conceptualization, writing – original draft, writing – review & editing, funding acquisition, and supervision.

Conflicts of interest

There are no conflicts to declare.

Acknowledgements

This work was funded by the NSFC (82172081 and 52103168), the Fundamental Research Funds for the Central Universities, and the Tianjin Applied Basic Research Multi-input Fund (21JCZDJC00970).

References

1 S. M. Park, A. Aalipour, O. Vermesh, J. H. Yu and S. S. Gambhir, *Nat. Rev. Mater.*, 2017, **2**, 17014.
2 E. A. Ashley, *Nat. Rev. Genet.*, 2016, **17**, 507.
3 A. Letai, *Nat. Med.*, 2016, **23**, 1028.
4 R. Weissleder, *Nat. Rev. Cancer*, 2012, **2**, 11.
5 J.-S. Ni, T. Min, Y. Li, M. Zha, P. Zhang, L. Ho and K. Li, *Angew. Chem., Int. Ed.*, 2020, **59**, 10179.
6 W. Li, Z. Yan, J. Ren and X. Qu, *Chem. Soc. Rev.*, 2018, **47**, 8639.
7 G. Hong, A. L. Antaris and H. Dai, *Nat. Biomed. Eng.*, 2017, **1**, 0010.
8 Z. Lei and F. Zhang, *Angew. Chem., Int. Ed.*, 2021, **60**, 16294.
9 G. Hong, S. Diao, J. Chang, A. L. Antaris, C. Chen, B. Zhang, S. Zhao, D. N. Atochin, P. L. Huang, K. I. Andreasson, C. J. Kuo and H. Dai, *Nat. Photonics*, 2014, **8**, 723.
10 A. L. Antaris, H. Chen, K. Cheng, Y. Sun, G. Hong, C. Qu, S. Diao, Z. Deng, X. Hu, B. Zhang, X. Zhang, O. K. Yaghi, Z. R. Alamparambil, X. Hong, Z. Cheng and H. Dai, *Nat. Mater.*, 2016, **15**, 235.
11 J. Qi, C. Sun, A. Zebibula, H. Zhang, R. T. K. Kwok, X. Zhao, W. Xi, J. W. Y. Lam, J. Qian and B. Z. Tang, *Adv. Mater.*, 2018, **30**, 1706856.
12 Y. Fan, P. Wang, Y. Lu, R. Wang, L. Zhou, X. Zheng, X. Li, J. A. Piper and F. Zhang, *Nat. Nanotechnol.*, 2018, **13**, 941.
13 C. Li, G. Chen, Y. Zhang, F. Wu and Q. Wang, *J. Am. Chem. Soc.*, 2020, **142**, 14789.
14 Z. Hu, C. Fang, B. Li, Z. Zhang, C. Cao, M. Cai, S. Su, X. Sun, X. Shi, C. Li, T. Zhou, Y. Zhang, C. Chi, P. He, X. Xia, Y. Chen, S. S. Gambhir, Z. Cheng and J. Tian, *Nat. Biomed. Eng.*, 2020, **4**, 259.
15 S. He, J. Song, J. Qu and Z. Cheng, *Chem. Soc. Rev.*, 2018, **47**, 4258.
16 H. Wan, J. Yue, S. Zhu, T. Uno, X. Zhang, Q. Yang, K. Yu, G. Hong, J. Wang, L. Li, Z. Ma, H. Gao, Y. Zhong, J. Su, A. L. Antaris, Y. Xia, J. Luo, Y. Liang and H. Dai, *Nat. Commun.*, 2018, **9**, 1171.
17 M. Zhang, J. Yue, R. Cui, Z. Ma, H. Wan, F. Wang, S. Zhu, Y. Zhou, Y. Kuang, Y. Zhong, D.-W. Pang and H. Dai, *Proc. Natl. Acad. Sci. U. S. A.*, 2018, **115**, 6590.
18 Kenry, Y. Duan and B. Liu, *Adv. Mater.*, 2018, **30**, 1802394.
19 W. Xu, D. Wang and B. Z. Tang, *Angew. Chem., Int. Ed.*, 2021, **60**, 7476.
20 Y. Liu, Y. Li, S. Koo, Y. Sun, Y. Liu, X. Liu, Y. Pan, Z. Zhang, M. Du, S. Lu, X. Qiao, J. Gao, X. Wang, Z. Deng, X. Meng, Y. Xiao, J. S. Kim and X. Hong, *Chem. Rev.*, 2022, **122**, 209.
21 Y. Liu, J. Liu, D. Chen, X. Wang, Z. Liu, H. Liu, L. Jiang, C. Wu and Y. Zou, *Macromolecules*, 2019, **52**, 5735.
22 T. Zhou, R. Hu, L. Wang, Y. Qiu, G. Zhang, Q. Deng, H. Zhang, P. Yin, B. Situ, C. Zhan, A. Qin and B. Z. Tang, *Angew. Chem., Int. Ed.*, 2020, **59**, 9952.
23 M. Verma, Y.-H. Chan, S. Saha and M.-H. Liu, *ACS Appl. Bio Mater.*, 2021, **4**, 2142.
24 G. Qian and Z. Y. Wang, *Chem. – Asian J.*, 2010, **5**, 1006.
25 C. Yin, H. Zhang, B. Sun, S. Chen, X. Jiang, X. Miao, P. Sun, W. Hu, Q. Fan and W. Huang, *Adv. Funct. Mater.*, 2021, **31**, 2106575.
26 J. Mu, M. Xiao, Y. Shi, X. Geng, H. Li, Y. Yin and X. Chen, *Angew. Chem., Int. Ed.*, 2022, **61**, e202114722.
27 S. Xu, H. Dai, S. Zhu, Y. Wu, M. Sun, Y. Chen, K. Fan, C. Zhang, C. Wang and W. Hu, *eScience*, 2021, **1**, 60.
28 C. Xu, Y. Jiang, Y. Han, K. Pu and R. Zhang, *Adv. Mater.*, 2021, **33**, 2008061.
29 W. Li, J. Zhang, Z. Gao, J. Qi and D. Ding, *Coord. Chem. Rev.*, 2022, **471**, 214754.
30 J. Li, R. Jiang, Q. Wang, X. Li, X. Hu, Y. Yuan, X. Lu, W. Wang, W. Huang and Q. Fan, *Biomaterials*, 2019, **217**, 119304.
31 X. Zhang, Y. Yang, T. Kang, J. Wang, G. Yang, Y. Yang, X. Lin, L. Wang, K. Li, J. Liu and J.-S. Ni, *Small*, 2021, **17**, 2100501.
32 Y. Wang, T. Hasegawa, H. Matsumoto, T. Mori and T. Michinobu, *Adv. Funct. Mater.*, 2017, **27**, 1701486.
33 D. Meng, R. Zheng, Y. Zhao, E. Zhang, L. Dou and Y. Yang, *Adv. Mater.*, 2022, **34**, 2107330.
34 P. Sun, X. Jiang, B. Sun, H. Wang, J. Li, Q. Fan and W. Huang, *Biomaterials*, 2022, **280**, 121319.
35 S. Xue, X. Qiu, Q. Sun and W. Yang, *J. Mater. Chem. C*, 2016, **4**, 1568.

36 T. R. Hopper, D. Qian, L. Yang, X. Wang, K. Zhou, R. Kumar, W. Ma, C. He, J. Hou, F. Gao and A. A. Bakulin, *Chem. Mater.*, 2019, **31**, 6860.
37 J. Li, L. Gao, T. Lu, Z. Feng, D. Jiang, C. Du, K. Wang, P. Lu and B. Zou, *Adv. Opt. Mater.*, 2021, **9**, 2100813.
38 S. Song, Y. Zhao, M. Kang, Z. Zhang, Q. Wu, S. Fu, Y. Li, H. Wen, D. Wang and B. Z. Tang, *Adv. Funct. Mater.*, 2021, **31**, 2107545.
39 C. Ji, W. Cheng, Q. Yuan, K. Müllen and M. Yin, *Acc. Chem. Res.*, 2019, **52**, 2266.
40 Q. Zhang, S. Dong, M. Zhang and F. Huang, *Aggregate*, 2021, **2**, 35.
41 Z. Zhang, X. Fang, Z. Liu, H. Liu, D. Chen, S. He, J. Zheng, B. Yang, W. Qin, X. Zhang and C. Wu, *Angew. Chem., Int. Ed.*, 2020, **59**, 3691.
42 X. Zhen, K. Pu and X. Jiang, *Small*, 2021, **17**, 2004723.
43 Y. Hong, J. W. Y. Lam and B. Z. Tang, *Chem. Soc. Rev.*, 2011, **40**, 5361.
44 S. Chen, H. Miao, X. Jiang, P. Sun, Q. Fan and W. Huang, *Biomaterials*, 2021, **275**, 120916.
45 Y.-X. Li, S.-P. Su, C.-H. Yang, M.-H. Liu, P.-H. Lo, Y.-C. Chen, C.-P. Hsu, Y.-J. Lee, H. K. Chiang and Y.-H. Chan, *Adv. Healthcare Mater.*, 2021, **10**, 2100993.
46 S. Naghibi, T. Chen, A. J. Ghahfarokhi and Y. Tang, *Aggregate*, 2021, **2**, e41.
47 Z. Zhao, H. Zhang, J. W. Y. Lam and B. Z. Tang, *Angew. Chem., Int. Ed.*, 2020, **59**, 9888.
48 W.-C. Chen, P.-T. Chou and Y.-C. Cheng, *J. Phys. Chem. C*, 2019, **123**, 10225.
49 Z. Xu, Y. Jiang, M. Fan, S. Tang, M. Liu, W.-C. Law, C. Yang, M. Ying, M. Ma, B. Dong, K.-T. Yong and G. Xu, *Adv. Opt. Mater.*, 2021, **9**, 2100859.
50 Y. Sun, P. Sun, Z. Li, L. Qu and W. Guo, *Chem. Soc. Rev.*, 2022, **51**, 7170.
51 Z. Zhang, W. Xu, M. Kang, H. Wen, H. Guo, P. Zhang, L. Xi, K. Li, L. Wang, D. Wang and B. Z. Tang, *Adv. Mater.*, 2020, **32**, 2003210.
52 Y. Jiang and K. Pu, *Acc. Chem. Res.*, 2018, **51**, 1840.
53 J. Qi, H. Ou, Q. Liu and D. Ding, *Aggregate*, 2021, **2**, 95.
54 W. Xu, Z. Zhang, M. Kang, H. Guo, Y. Li, H. Wen, M. M. S. Lee, Z. Wang, R. T. K. Kwok, J. W. Y. Lam, K. Li, L. Xi, S. Chen, D. Wang and B. Z. Tang, *ACS Mater. Lett.*, 2020, **2**, 1033.
55 R. Jiang, J. Dai, X. Dong, Q. Wang, Z. Meng, J. Guo, Y. Yu, S. Wang, F. Xia, Z. Zhao, X. Lou and B. Z. Tang, *Adv. Mater.*, 2021, **33**, 2101158.
56 W. Wu, D. Mao, S. Xu, F. Kenry, X. Hu, D. Li, B. Kong and B. Liu, *Chem*, 2018, **4**, 1937.
57 J. Qi, S. Jia, X. Kang, X. Wu, Y. Hong, K. Shan, X. Kong, Z. Wang and D. Ding, *Adv. Mater.*, 2022, **34**, 2203309.
58 J. Mu, M. Xiao, Y. Shi, X. Geng, H. Li, Y. Yin and X. Chen, *Angew. Chem., Int. Ed.*, 2022, **61**, e202114722.
59 M. Verma, Y.-H. Chan, S. Saha and M.-H. Liu, *ACS Appl. Bio Mater.*, 2021, **4**, 2142.
60 H. Dai, X. Wang, J. Shao, W. Wang, X. Mou and X. Dong, *Small*, 2021, **17**, 2102646.
61 D. Gao, D. Hu, X. Liu, X. Zhang, Z. Yuan, Z. Sheng and H. Zheng, *ACS Appl. Polym. Mater.*, 2020, **2**, 4241.
62 M. Yang, J. Huang, J. Fan, J. Du, K. Pu and X. Peng, *Chem. Soc. Rev.*, 2020, **49**, 6800.
63 S. Zhu, R. Tian, A. L. Antaris, X. Chen and H. Dai, *Adv. Mater.*, 2019, **31**, 1900321.
64 Z. Shi, X. Han, W. Hu, H. Bai, B. Peng, L. Ji, Q. Fan, L. Li and W. Huang, *Chem. Soc. Rev.*, 2020, **49**, 7533.
65 A. Ji, H. Lou, C. Qu, W. Lu, Y. Hao, J. Li, Y. Wu, T. Chang, H. Chen and Z. Cheng, *Nat. Commun.*, 2022, **13**, 3815.
66 G. Hong, Y. Zou, A. L. Antaris, S. Diao, D. Wu, K. Cheng, X. Zhang, C. Chen, B. Liu, Y. He, J. Z. Wu, J. Yuan, B. Zhang, Z. Tao, C. Fukunaga and H. Dai, *Nat. Commun.*, 2014, **5**, 4206.
67 B. Liu, X. Chen, Y. Zou, Y. He, L. Xiao, X. Xu, L. Li and Y. Li, *Polym. Chem.*, 2013, **4**, 470.
68 L. Feng, C. Li, L. Liu, X. Chen, G. Jiang, J. Wang and B. Z. Tang, *Angew. Chem., Int. Ed.*, 2022, **61**, e202212673.
69 A. Tang, C. Zhan, J. Yao and E. Zhou, *Adv. Mater.*, 2017, **29**, 1600013.
70 W. Li, K. H. Hendriks, M. M. Wienk and R. A. J. Janssen, *Acc. Chem. Res.*, 2016, **49**, 78.
71 K. Shou, Y. Tang, H. Chen, S. Chen, L. Zhang, A. Zhang, Q. Fan, A. Yu and Z. Cheng, *Chem. Sci.*, 2018, **9**, 3105.
72 Y. Liu, J. Liu, D. Chen, X. Wang, Z. Zhang, Y. Yang, L. Jiang, W. Qi, Z. Ye, S. He, Q. Liu, L. Xi, Y. Zou and C. Wu, *Angew. Chem., Int. Ed.*, 2020, **59**, 21049.
73 Q. Zhang, M. A. Kelly, N. Bauer and W. You, *Acc. Chem. Res.*, 2017, **50**, 2401.
74 C. Li, G. Jiang, J. Yu, W. Ji, L. Liu, P. Zhang, J. Du, C. Zhan, J. Wang and B. Z. Tang, *Adv. Mater.*, 2023, **35**, 2208229.
75 D. Chen, Y. Liu, Z. Zhang, Z. Liu, X. Fang, S. He and C. Wu, *Nano Lett.*, 2021, **21**, 798.
76 S. Wang, Y. Fan, D. Li, C. Sun, Z. Lei, L. Lu, T. Wang and F. Zhang, *Nat. Commun.*, 2019, **10**, 1058.
77 X. Zhao, F. Zhang and Z. Lei, *Chem. Sci.*, 2022, **13**, 11280.
78 H. Zhou, Z. Lu, Y. Zhang, M. Li, D. Xue, D. Zhang, J. Liu, L. Li, J. Qian and W. Huang, *ACS Appl. Mater. Interfaces*, 2022, **14**, 8705.
79 M.-H. Liu, Z. Zhang, Y.-C. Yang and Y.-H. Chan, *Angew. Chem., Int. Ed.*, 2021, **60**, 983.
80 J. Qi, X. Duan, W. Liu, Y. Li, Y. Cai, J. W. Y. Lam, R. T. K. Kwok, D. Ding and B. Z. Tang, *Biomaterials*, 2020, **248**, 120036.
81 C. Chen, X. Ni, S. Jia, Y. Liang, X. Wu, D. Kong and D. Ding, *Adv. Mater.*, 2019, **31**, 1904914.
82 H. Piwonski, W. Li, Y. Wang, T. Michinobu and S. Habuchi, *ACS Appl. Polym. Mater.*, 2020, **2**, 569.
83 L. Yuan, K. Lu, B. Xia, J. Zhang, Z. Wang, Z. Wang, D. Deng, J. Fang, L. Zhu and Z. Wei, *Adv. Mater.*, 2016, **28**, 5980.
84 S. Liu, H. Ou, Y. Li, H. Zhang, J. Liu, X. Lu, R. T. K. Kwok, J. W. Y. Lam, D. Ding and B. Z. Tang, *J. Am. Chem. Soc.*, 2020, **142**, 15146.
85 Z. Zhang, X. Fang, Z. Liu, H. Liu, D. Chen, S. He, J. Zheng, B. Yang, W. Qin, X. Zhang and C. Wu, *Angew. Chem., Int. Ed.*, 2020, **59**, 3691.

86 L. Yao, S. Zhang, R. Wang, W. Li, F. Shen, B. Yang and Y. Ma, *Angew. Chem., Int. Ed.*, 2014, **53**, 2119.
87 M. F. Kircher, A. D. L. Zerda, J. V. Jokerst, C. L. Zavaleta, P. J. Kempen, E. Mittra, K. Pitter, R. M. Huang, C. Campos, F. Habte, R. Sinclair, C. W. Brennan, I. K. Mellinghoff, E. C. Holland and S. S. Gambhir, *Nat. Med.*, 2012, **18**, 829.
88 K. Heinzmann, L. M. Carter, J. S. Lewis and E. O. Aboagye, *Nat. Biomed. Eng.*, 2017, **1**, 697.
89 L. V. Wang and S. Hu, *Science*, 2012, **335**, 1458.
90 K. Pu, A. J. Shuhendler, J. V. Jokerst, J. Mei, S. S. Gambhir, Z. Bao and J. Rao, *Nat. Nanotechnol.*, 2014, **9**, 233.
91 J. Weber, P. C. Beard and S. E. Bohndiek, *Nat. Methods*, 2016, **13**, 639.
92 J. Qi, C. Chen, X. Zhang, X. Hu, S. Ji, R. T. K. Kwok, J. W. Y. Lam, D. Ding and B. Z. Tang, *Nat. Commun.*, 2018, **9**, 1848.
93 H. Gao, X. Duan, D. Jiao, Y. Zeng, X. Zheng, J. Zhang, H. Ou, J. Qi and D. Ding, *Angew. Chem., Int. Ed.*, 2021, **60**, 21047.
94 B. Guo, Z. Feng, D. Hu, S. Xu, E. Middha, Y. Pan, C. Liu, H. Zheng, J. Qian, Z. Sheng and B. Liu, *Adv. Mater.*, 2019, **31**, 1902504.
95 Y. Yang, X. Fan, L. Li, Y. Yang, A. Nuernisha, D. Xue, C. He, J. Qian, Q. Hu, H. Chen, J. Liu and W. Huang, *ACS Nano*, 2020, **14**, 2509.
96 American National Standards Institute, *Z136.1–2007 American National Standard for Safe Use of Lasers*, New York, 2007.
97 C. Yin, X. Li, Y. Wang, Y. Liang, S. Zhou, P. Zhao, C.-S. Lee, Q. Fan and W. Huang, *Adv. Funct. Mater.*, 2021, **31**, 2104650.
98 B. Tang, W.-L. Li, Y. Chang, B. Yuan, Y. Wu, M.-T. Zhang, J.-F. Xu, J. Li and X. Zhang, *Angew. Chem., Int. Ed.*, 2019, **58**, 15526.
99 M. E. Davis, *Clin. J. Oncol. Nurs.*, 2016, **20**, S2.
100 M. Weller, M. van den Bent, M. Preusser, E. Le Rhun, J. C. Tonn, G. Minniti, M. Bendszus, C. Balana, O. Chinot, L. Dirven, P. French, M. E. Hegi, A. S. Jakola, M. Platten, P. Roth, R. Rudà, S. Short, M. Smits, M. J. B. Taphoorn, A. von Deimling, M. Westphal, R. Soffietti, G. Reifenberger and W. Wick, *Nat. Rev. Clin. Oncol.*, 2021, **18**, 170.
101 M. Lara-Velazquez, R. Al-Kharboosh, S. Jeanneret, C. Vazquez-Ramos, D. Mahato, D. Tavanaiepour, G. Rahmathulla and A. Quinones-Hinojosa, *Brain Sci.*, 2017, **7**, 166.
102 C. D. Arvanitis, G. B. Ferraro and R. K. Jain, *Nat. Rev. Cancer*, 2020, **20**, 26.
103 L. Chiossone, P. Y. Dumas, M. Vienne and E. Vivier, *Nat. Rev. Immunol.*, 2018, **18**, 671.
104 G. Deng, X. Peng, Z. Sun, W. Zheng, J. Yu, L. Du, H. Chen, P. Gong, P. Zhang, L. Cai and B. Z. Tang, *ACS Nano*, 2020, **14**, 11452.
105 M. Rybiński, Z. Szymańska, S. Lasota and A. Gambin, *J. R. Soc., Interface*, 2013, **10**, 20130527.
106 Y. Song, Y. Wang, Y. Zhu, Y. Cheng, Y. Wang, S. Wang, F. Tan, F. Lian and N. Li, *Adv. Healthcare Mater.*, 2019, **8**, 1900250.
107 M. Chang, Z. Hou, D. Jin, J. Zhou, M. Wang, M. Wang, M. Shu, B. Ding, C. Li and J. Lin, *Adv. Mater.*, 2020, **32**, 2004647.
108 X. Tang, L. Tan, K. Shi, J. Peng, Y. Xiao, W. Li, L. Chen, Q. Yang and Z. Qian, *Acta Pharm. Sin. B*, 2018, **8**, 587.
109 G. Ma, Z. Liu, C. Zhu, H. Chen, R. T. K. Kwok, P. Zhang, B. Z. Tang, L. Cai and P. Gong, *Angew. Chem.*, 2022, **134**, e202207213.
110 Q. Gao, X. Zhang, W. Yin, D. Ma, C. Xie, L. Zheng, X. Dong, L. Mei, J. Yu, C. Wang, Z. Gu and Y. Zhao, *Small*, 2018, **14**, 1802290.
111 C. Szabó, H. Ischiropoulos and R. Radi, *Nat. Rev. Drug Discovery*, 2007, **6**, 662.
112 X. Kang, Y. Li, S. Yin, W. Li and J. Qi, *Biosensors*, 2022, **12**, 646.
113 J. Li, L. Xie, B. Li, C. Yin, G. Wang, W. Sang, W. Li, H. Tian, Z. Zhang, X. Zhang, Q. Fan and Y. Dai, *Adv. Mater.*, 2021, **33**, 2008481.
114 C. Su, Y. Liu, R. Li, W. Wu, J. P. Fawcett and J. Gu, *Adv. Drug Delivery Rev.*, 2019, **143**, 97.
115 J. Pellico, P. J. Gawne and R. T. M. de Rosales, *Chem. Soc. Rev.*, 2021, **50**, 3355.
116 D. Wei, Y. Yu, Y. Huang, Y. Jiang, Y. Zhao, Z. Nie, F. Wang, W. Ma, Z. Yu, Y. Huang, X.-D. Zhang, Z.-Q. Liu, X. Zhang and H. Xiao, *ACS Nano*, 2021, **15**, 5428.
117 D. Tang, Y. Yu, J. Zhang, X. Dong, C. Liu and H. Xiao, *Adv. Mater.*, 2022, **34**, 2203820.